ACS Photonics

Open Access

This article is licensed under CC-BY 4.0

pubs.acs.org/journal/apchd5

Letter

Metasurface-Controlled Holographic Microcavities

Sydney Mason, Maryna Leonidivna Meretska, Christina Spägele, Marcus Ossiander,* and Federico Capasso

Cite This: *ACS Photonics* 2024, 11, 941−949

Read Online

ACCESS | Metrics & More | Article Recommendations

ABSTRACT: Optical microcavities confine light to wavelength-scale volumes and are a key component for manipulating and enhancing the interaction of light, vacuum states, and matter. Current microcavities are constrained to a small number of spatial mode profiles. Imaging cavities can accommodate complicated modes but require an externally preshaped input. Here, we experimentally demonstrate a visible-wavelength, metasurface-based holographic microcavity that overcomes these limitations. The micrometer-scale metasurface cavity fulfills the round-trip condition for a designed mode with a complex-shaped intensity profile and thus selectively enhances light that couples to this mode, achieving a spectral bandwidth of 0.8 nm. By imaging the intracavity mode, we show that the holographic mode changes quickly with the cavity length and that the cavity displays the desired spatial mode profile only close to the design cavity length. When a metasurface is placed on a distributed Bragg reflector and steep phase gradients are realized, the correct choice of the reflector's top layer material can boost metasurface performance considerably. The applied forward-design method can be readily transferred to other spectral regimes and mode profiles.

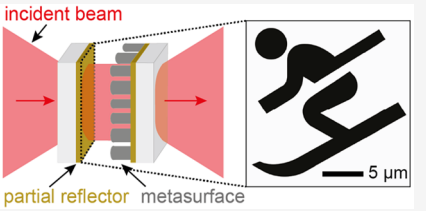

KEYWORDS: *metaoptics, photonic cavity, hologram, optical metamaterials, mode shaping*

Downloaded via HARVARD UNIV on May 29, 2024 at 02:29:48 (UTC).
See https://pubs.acs.org/sharingguidelines for options on how to legitimately share published articles.

INTRODUCTION

Optical cavities trap light and are useful for applications in linear, nonlinear, and quantum optics, metrology, communications, and computing.[1] Microscale cavities, with mode volumes on the order of a few wavelengths cubed, additionally provide precise control over the state and evolution of matter within them.[2−4] For example, cavities for the detection of molecules[5] and the imaging of nanoparticles[6] have been developed, and cavity quantum electrodynamics has been exploited to trap and manipulate single atoms.[7] This makes optical cavities good candidates for applications in quantum networks and nanoscale sensing.[8] So far, most cavities are designed using conventional optics and thus support a limited number of simple spatial mode profiles.[9,10] Special cavity geometries can exhibit imaging properties,[11−13] which provide field enhancement for designed mode profiles. However, their size is on the order of millimeters, and they require the external injection of the desired mode profile.[13]

Optical metasurfaces allow control of the intensity, polarization, and phase of light on the subwavelength scale[14−16] and can be used, e.g., as polarizers, modulators, surface wave absorbers, waveguides,[15] and objective lenses.[17] High-fidelity computer-generated holography is another important metasurface use case[18−20] with applications in augmented reality,[21] security, and encryption.[22] Metasurfaces have so far been used to counteract the transverse mode expansion in cavities and so to provide stable microcavities without concave mirrors at microwave frequencies,[23] at telecom wavelengths,[24] for external cavity lasers,[19] and within hollow-core fibers[25] but not in the visible spectrum with free-space cavities. Additionally, the large phase response and spectral control provided by metasurfaces have allowed for nanoscale cavities on the order of a metaatom.[26,27] Metasurface cavities have been designed to achieve a near-zero index allowing for on-chip phase matching.[26] This approach can be used to enhance integrated photonic platforms. Other approaches to metasurface optical cavities exploit metasurfaces for decreasing the cavity size,[27] steering the mode exiting the cavity,[28,29] and altering the cavity spectrum.[27,30,31]

This selection demonstrates the impressive versatility of metasurface microcavities and their multifarious applications, many of which accept or even require a broadband cavity response. However, other applications, e.g., field enhancement, demand cavities with narrow spectral resonances. To achieve a cavity mode with a narrow line width, its transverse phase evolution must be carefully controlled every time light propagates a full round-trip in the cavity.

Recently, two works have shown such transverse phase control using metasurfaces and have experimentally demonstrated stable Gaussian modes in microcavities.[23,24] For

Received: October 12, 2023
Revised: January 30, 2024
Accepted: January 30, 2024
Published: February 15, 2024

© 2024 The Authors. Published by American Chemical Society

Gaussian-shaped modes, the metasurface approaches have not yet exceeded the capabilities of state-of-the-art microscale spherical mirrors.[9] However, metasurfaces can realize considerably steeper phase gradients than microscale mirrors which are limited by cracks that form during their fabrication if their topography changes quickly.[9]

Due to their ability for sub-wavelength phase control, metasurfaces have been predicted to allow intracavity microscale holography,[24] i.e., stable cavity modes with a complicated spatial profile. So far, the idea has been theoretically explored only for infrared light. However, the approach has not yet been experimentally demonstrated.

Here we fill this gap and experimentally create an open metasurface microcavity operating in the visible range ($\lambda = 633$ nm). Through a computer-generated holography design approach, the miniaturized optical cavity creates a complex-shaped intracavity mode that classical optics cannot achieve. Its spatial profile can be nonspherical and asymmetrical and can comprise multiple narrow or differing features.

While previous work on metasurface optical microcavities[27,30,31] has exploited metasurfaces to control the spectral characteristics of cavity resonances and to shape the output of cavities,[19,28,29] here we for the first time experimentally realize a stable cavity mode with a complicated spatial profile inside the cavity. We image the cavity-length-dependent microscale intracavity mode experimentally and demonstrate that the concept synthesizes the designed transverse mode at a specific cavity length.

METHODS

The setup of our metasurface microcavity is shown in Figure 1a: it consists of two opposing, flat partial reflectors with a metasurface placed on one of the reflectors. This setup resembles a plano-concave cavity, with the metasurface taking the role of the spherical mirror. As indicated in Figure 1a, from now on we will label the top of the uncovered partial reflector (PR) as the image plane (IP) and the top of the metasurface-covered reflector (MS) as the metasurface plane (MP).

For a mode to build up in the cavity, the phase and intensity profiles of the mode must reproduce after each round-trip, i.e., for each transverse position (x, y) in the metasurface plane, the round-trip phase $\Delta\phi(x, y)$ accrued by the light within the cavity is an integer multiple q of 2π.[32] The contributions to $\Delta\phi$ are the mode's propagation phase from the image plane to the metasurface plane $\phi_{\mathrm{IP}\to\mathrm{MP}}^{\mathrm{forward}}$, the spatially dependent metasurface reflection phase ϕ_{MS}, the mode's propagation phase back to the image plane $\phi_{\mathrm{MP}\to\mathrm{IP}}^{\mathrm{forward}}$, and the spatially independent reflection phase of the partial reflector ϕ_{PR}:

$$\Delta\phi(x, y) = 2\pi q = \phi_{\mathrm{IP}\to\mathrm{MP}}^{\mathrm{forward}} + \phi_{\mathrm{MS}} + \phi_{\mathrm{MP}\to\mathrm{IP}}^{\mathrm{forward}} + \phi_{\mathrm{PR}} \tag{1}$$

When we explicitly include the spatial dependence, all phase contributions must be treated in a single plane, i.e., the metasurface plane. Therefore, we replace the forward propagation phase from the metasurface plane to the image plane $\phi_{\mathrm{MP}\to\mathrm{IP}}^{\mathrm{forward}}(x', y')$ with $-\phi_{\mathrm{IP}\to\mathrm{MP}}^{\mathrm{backward}}(x, y)$. A full round-trip is then described by

$$\Delta\phi(x, y) = 2\pi q = \phi_{\mathrm{IP}\to\mathrm{MP}}^{\mathrm{forward}}(x, y) + \phi_{\mathrm{MS}}(x, y) - \phi_{\mathrm{IP}\to\mathrm{MP}}^{\mathrm{backward}}(x, y) + \phi_{\mathrm{PR}} \tag{2}$$

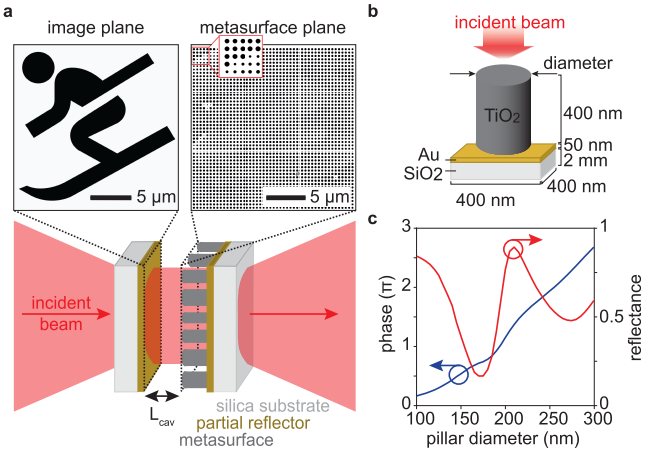

Figure 1. Holographic microcavity concept and design. (a) Holographic microcavity that forms an intracavity image: unstructured light is incident from the left. In the cavity, a metasurface (right inset) introduces a reflective phase profile that fulfills the round-trip phase resonance condition for a designed mode. Because light interferes constructively only if the round-trip condition is met, only the mode with the desired spatial intensity profile in the image plane (left inset) is excited in the cavity. The desired intensity profile is encoded in the metasurface as a phase-only hologram by suitable design of the nanopillars' phase shifts. For this demonstration, we chose a spatial mode profile resembling a skier. (b) Metaatom schematic used to create the nanopillar library in panel c. Light is incident normally on a circular titania (TiO_2) nanopillar which sits on a partially reflective gold (Au) layer on a thick fused silica (SiO_2) substrate. (c) Nanopillar library for visible light (633 nm). Whereas the gold layer controls the average reflectance (red line), the nanopillars' reflection phase (blue line) can be tuned by more than 2π via their diameter.

The propagation phases also depend on the length of the cavity L_{cav}, indicated in Figure 1a.

Metasurface Phase Calculation. To create a microcavity that selectively enhances a mode with a spatial intensity profile $I_{\mathrm{IP}}(x', y')$ in the image plane x', y', we design a metasurface that fulfills the round-trip condition for this mode profile.

Assuming a flat phase in the imaging plane, the complex electric field amplitude of the mode is proportional to the square root of its intensity $E_{\mathrm{IP}}(x', y') \sim \sqrt{I_{\mathrm{IP}}(x', y')}$. We can then calculate the evolution of this mode along the propagation direction z using the Rayleigh–Sommerfeld diffraction integral:[24]

$$E(x, y, z, k) = -\frac{ik}{2\pi}\int\int \mathrm{d}x'\,\mathrm{d}y'\, E_{\mathrm{IP}}(x', y')\frac{\mathrm{e}^{\pm ikr}}{r}\cos(\chi) \tag{3}$$

$$r = \sqrt{(x - x')^2 + (y - y')^2 + z^2} \tag{4}$$

$$\chi = \tan^{-1}\left(\frac{\sqrt{(x - x')^2 + (y - y')^2}}{z}\right) \tag{5}$$

The equation describes how the metasurface is designed: we search for a metasurface phase that fulfills the round-trip condition for an already known image $I_{\mathrm{IP}}(x', y')$. In eq 3, we use the positive propagator for forward propagation and the negative propagator for backward propagation. The phase difference between the forward-propagated mode field $E_{\mathrm{IP}\to\mathrm{MP}}^{\mathrm{forward}}(x, y)$ and the backward-propagated mode field $E_{\mathrm{IP}\to\mathrm{MP}}^{\mathrm{backward}}(x, y)$ then

https://doi.org/10.1021/acsphotonics.3c01479
ACS Photonics 2024, 11, 941−949

represents the round-trip propagation phase without the reflector phases (see eq 2):

$$\phi_{\mathrm{IP}\to\mathrm{MP}}^{\mathrm{forward}}(x, y) - \phi_{\mathrm{IP}\to\mathrm{MP}}^{\mathrm{backward}}(x, y) = \arg(E_{\mathrm{IP}\to\mathrm{MP}}^{\mathrm{forward}}(x, y)) - \arg(E_{\mathrm{IP}\to\mathrm{MP}}^{\mathrm{backward}}(x, y)) \quad (6)$$

Consequently, we can fulfill the round-trip condition eq 2 for a designer mode with an intensity profile $I_{\mathrm{IP}}(x', y')$ with a metasurface that realizes a spatial phase profile:

$$\phi_{\mathrm{MS}}(x, y) = 2\pi q - \arg(E_{\mathrm{IP}\to\mathrm{MP}}^{\mathrm{forward}}(x, y)) + \arg(E_{\mathrm{IP}\to\mathrm{MP}}^{\mathrm{backward}}(x, y)) - \phi_{\mathrm{PR}} \quad (7)$$

Because ϕ_{PR} is spatially independent, we neglect it in the following.

To demonstrate this design concept's capability for adapting an arbitrary mode profile, we chose a skier shape (Figure 1a, inset) as the designed mode profile. The shape exhibits small features with bars as narrow as 1.5 μm. Furthermore, we chose an operating wavelength of 633 nm, a cavity mirror reflectance of 50%, a metasurface size of 20 μm × 20 μm, and a cavity length of 40 μm. The finite transverse size limits the effective numerical aperture of our cavity, that is, the maximum transverse momentum components of light that can be trapped by it. This, in turn, limits the steepness of the intensity gradients realizable in such a cavity. The effect of the finite cavity size is illustrated in Figure 4a, which still shows the desired mode with high fidelity.

Metasurface Cavity Design. Our metaatom schematic is pictured in Figure 1b: as this demonstration does not require the high reflectances of distributed Bragg reflectors (DBRs), which are typically used to realize cavities with high finesses,[33] we used metallic partial reflectors, which allow easy tuning of the reflectance via the metal thickness. We use a 50 nm thick layer of gold on the fused silica substrates for the cavity-end reflectors, which resulted in 46% reflectance at 633 nm. We chose titania nanopillars as metaatoms because of titania's low absorption and high refractive index in the visible range.[34] We then created a reflectance library of metaatoms through finite-difference time-domain modeling (Lumerical FDTD) of nanopillars with a constant height (400 nm), a constant periodicity (400 nm × 400 nm), and diameters ranging from 100 to 300 nm. The resulting library is shown in Figure 1c and allows changes of the reflection phase by more than 2π with an average 57% reflectance across the nanopillar distribution.

We calculate the evolution of the skier mode within the cavity using eq 3 and discretize the phase resulting from eq 7 into 400 nm × 400 nm cells; see Figure 2a. Metaatoms with the corresponding phases are selected from the library and mapped to each cell to build the metasurface design. The inset in Figure 1a shows a top view of the final metasurface design.

The final performance of the metasurface cavity depends on the wavelength, the cavity length and transverse size, the employed materials and reflectors, fabrication quality, and principally the complexity of the desired mode profile. Extreme gradients in the pillar diameter, caused, e.g., by very narrow features in the mode profile or high numerical apertures, impact the holographic cavity's performance. Carefully selecting the metaatoms such that their pillar sizes change slowly in the center of the metasurface improves performance.[24] Although the choice of the mode profile for this demonstration, the skier, is subject to such limitations, we show the robustness of this design platform by choosing a complex spatial mode. In practice, the performance of the device will, to some extent, depend on the choice of the hologram and application.

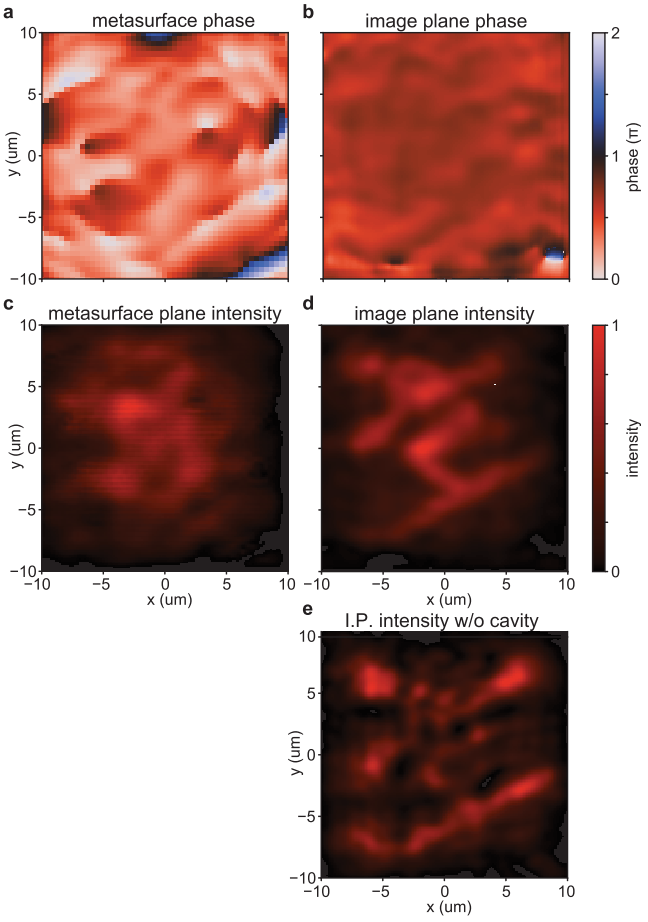

Figure 2. Evolution from the spatial phase profile to the designed spatial intensity profile. (a) Reflection phase of the metasurface. (b) Modeled phase profile of the excited mode in the image plane. The simulation shows only a minimal phase variation in the image plane. (c) Intensity profile of the excited mode in the metasurface plane (modeled). In the metasurface plane, the excited mode does not resemble the incoming plane wave nor does it resemble the designed skier intensity profile. (d) In the image plane, the modeled excited mode intensity profile resembles the designed skier shape. (e) Image quality strongly deteriorates when only reflection from the metasurface partial reflector is modeled without a second partial reflector to form the cavity.

Contrary to common holography algorithms,[35] designing cavity holograms using the resonance condition (eq 1) requires no iteration. The design flow is as follows:

(1) choose the spatial profile of the desired mode $E_{\mathrm{IP}}(x', y')$, the design wavelength, and the cavity dimensions, based on the desired image $I_{\mathrm{IP}}(x', y')$;
(2) identify the reflector type, e.g., metallic reflector or DBR (see section "DBR Subtleties in Metasurface Micro-cavities" on favorable DBR characteristics) and the metasurface material;
(3) calculate a metaatom library, i.e., the nanopillar diameter-dependent reflection phase for the chosen reflector and metasurface material, and adapt the transverse unit cell size and nanopillar height to achieve full phase coverage;
(4) use eqs 3 and 7 to calculate the metasurface phase $\phi_{\mathrm{MS}}(x, y)$ from $E_{\mathrm{IP}}(x', y')$;

https://doi.org/10.1021/acsphotonics.3c01479
ACS Photonics 2024, 11, 941−949

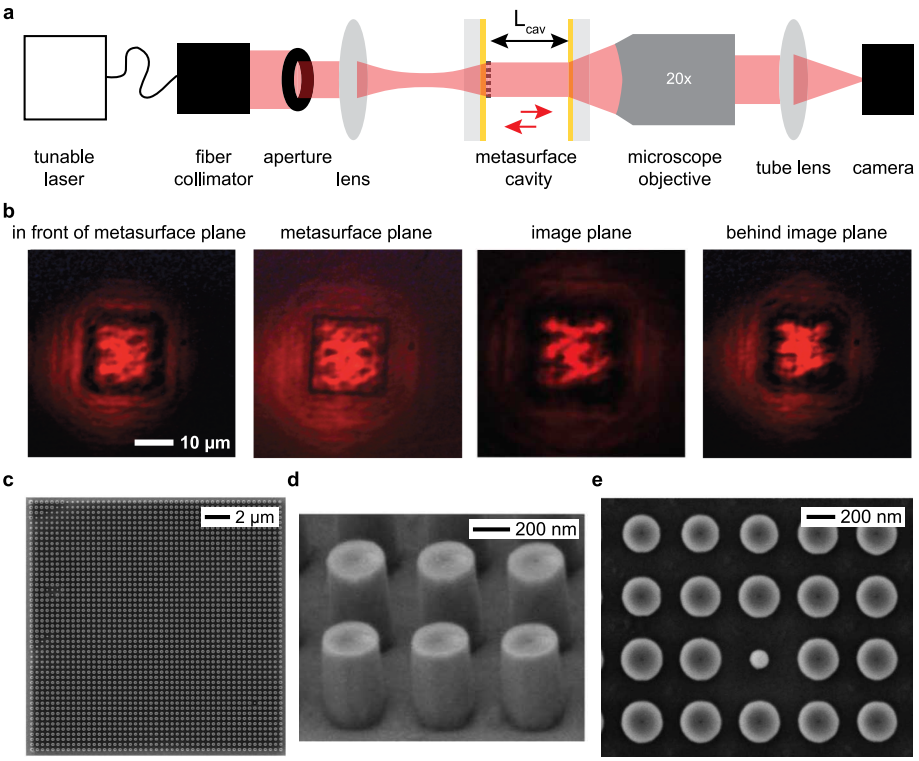

Figure 3. Experimental demonstration of a holographic microcavity. (a) Optical measurement setup. Light from a tunable laser is coupled to the metasurface cavity by a lens. The beam size is reduced by an aperture. Using a microscope objective and a camera, we image the transverse mode profile for different cavity lengths (imaged by changing L_{cav}, controlled by a piezo stage, data in Figure 4) and different transverse planes along the optical axis (imaged by shifting the focal plane of the microscope objective, data in panel b). Simultaneously, we measure the transmitted light's spectrum using a beam splitter between the objective and tube lens and a spectrometer (data in Figure 4). The planes are along the optical axis and parallel to the metasurface and are imaged by shifting the focus of the microscope objective through the cavity. (b) Formation of the intracavity hologram. The four images show the transverse mode profile at different positions along the optical axis. During the measurement, the cavity length remained fixed. The four images depict the transverse mode profiles in a plane ~40 μm in front of the microcavity, in the plane of the metasurface, in the image plane, and in a plane ~40 μm behind the cavity. It is apparent that the mode profile only resembles the skier in the image plane. The images were captured by scanning the microscope objective's focal plane along the optical axis. The scale bar applies to all four images. (c) Scanning electron microscope (SEM) image of the entire metasurface. (d) SEM side profile image of the nanopillars in the metasurface (400 nm in height). (e) SEM image of a subsection of the metasurface, showing pillar diameter variation.

(5) discretize $\phi_{MS}(x, y)$ using the transverse unit cell dimensions and map the phase in each position to a pillar diameter to obtain the metasurface design.

Numeric Validation. After designing the metasurface phase profile and the metacavity, we validated the full cavity using finite-difference time-domain simulations (Flexcompute, Tidy3d, https://www.flexcompute.com/). We simulate the full metasurface cavity volume, circumscribed with perfectly matched layers in the propagation direction placed one wavelength before the entrance metallic partial reflector and one wavelength after the exit partial reflector of the microcavity.

In the simulation, we find the best representation of the skier in the image plane with a cavity length of ~37.0 μm, slightly shorter than our design length. This shift is caused by light penetration into the metasurface and the partial reflector, which changes the imaging condition. The effect has been previously observed for spherical microcavities.[23,24] Without a second partial reflector, i.e., without a cavity, the metasurface creates only a poor representation of the skier, because the spatial intensity profile is uncontrolled.

This is verified by the simulation in Figure 2e, which shows the intensity profile generated by the metasurface upon a single reflection. When the second partial reflector is added and the cavity is closed, only the light that couples into the skier mode fulfills the round-trip condition. As a consequence, this light interferes constructively every round-trip, leading to field enhancement and intensity build-up in the skier mode (Figure 2d).

Figure 2b shows that the phase profile in the image plane barely varies, in accordance with the spatially constant phase profile in the image plane that we chose during the design process. Figure 2c shows the intensity profile of the fully built-up skier mode in the metasurface plane of the cavity, which is not similar to the skier.

Cavity Mirror and Metasurface Fabrication. For the experimental realization of the cavity, we first fabricated two partial reflectors by depositing a chromium adhesion layer (5 nm) and a partially reflective gold film (50 nm) on fused silica substrates via electron-beam evaporation. Using plasma-enhanced chemical vapor deposition, we deposited a thin fused silica layer on one of the reflectors to aid the adhesion of the titania nanopillars to the gold. The titania metasurface was then fabricated on this sample following a previously presented approach:[34] the sample was coated with positive electron beam lithography resist (Zeon Corporation, ZEP-520A), baked, and covered with a conductive polymer layer (Showa Denko, ESPACER) to prevent charging effects. Electron-beam lithography was used to define a negative of the metasurface layout

https://doi.org/10.1021/acsphotonics.3c01479
ACS Photonics 2024, 11, 941−949

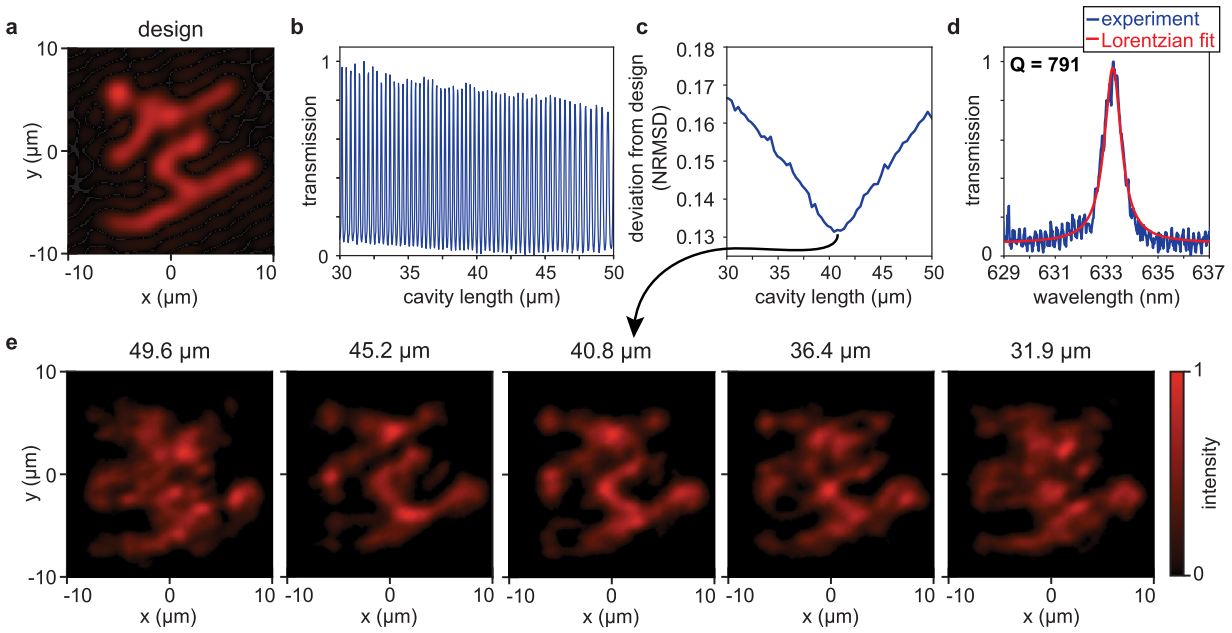

Figure 4. Tuning of the microcavity mode. (a) Spatial intensity profile of the target mode filtered such that it only contains transverse wavevectors that are supported by the finite cavity dimensions (20 μm × 20 μm × 40 μm; transverse, transverse, longitudinal). All false-color plots share the color bar in panel e. (b) Cavity-length-dependent transmission of the cavity. (c) Cavity-length dependence of the normalized root-mean-square deviation (NRMSD) between the peak of the observed mode and that of the target mode. (d) Measured spectrally resolved transmission (blue line) at 40.8 μm cavity length and a Lorentzian fit (red line) to the experimental data. (e) Evolution of the spatial mode profile in the image plane when changing the cavity length. We experimentally observe the best-matching spatial cavity mode profile at a 40.8 μm cavity length, close to the design length of 40.0 μm.

after development in *o*-xylene. This negative layer was then filled with titania using atomic layer deposition, creating the nanopillars. Lastly, excess titania on top of the resist was removed by using reactive ion etching, and the resist was removed (MicroChem, Remover PG). Figure 3c–e shows scanning electron micrographs of the finished metasurface and close-ups of the nanopillar geometry.

Experimental Procedure. Figure 3a shows the experimental setup built to investigate the performance of the holographic microcavity. Light from a tunable laser (NKT Photonics, SuperK) is collimated into free space by a fiber collimator. Due to the small transverse size of the cavity, we weakly focus the incoming beam. To limit the resulting phase curvature of the incoming wavefront and uniformly illuminate the metasurface, we first reduce the size of the incoming beam to less than 0.5 mm using an aperture. Then, a focusing lens (focal length f = 3 cm) couples light into the cavity (resulting in a numerical aperture NA < 0.01).

The metasurface reflector sits on a piezo-driven three-axis stage (Thorlabs, Nanomax) to allow movement relative to the laser beam and to tune the cavity length. We couple light to the cavity from the metasurface plane side to allow imaging of the cavity mode in the image plane with a 20× microscope objective, a tube lens, and a camera. At the same time, we recorded the spectrum of the cavity mode using a beam splitter and grating spectrometer (Andor, Shamrock, not shown).

RESULTS

Experimental Results. When a laser beam is incident on the cavity and provided that the cavity is close to its design length and the cavity is on resonance, we observe that the skier mode is excited. As seen in Figure 3b, the shaped intensity profile builds up even though the cavity is illuminated by an unstructured beam. As expected, the skier intensity profile is only visible in the image plane, which we verified by scanning the microscope objective along the optical axis to image the mode profile at different longitudinal positions (Figure 3b): the metasurface plane is recognizable by its square shape; however, in this plane, no skier is observed. The same is true for positions in front and after the microcavity.

We then focused on the length tuning of the cavity mode: we fixed the microscope objective position to image the image plane onto the camera sensor and swept the cavity length by changing the position of the metasurface reflector (compare with Figure 3a). At each longitudinal position of the metasurface reflector, we recorded the transmitted spectrum with the laser tuned to 633 ± 35 nm (full width at half-maximum intensity bandwidth). The broad bandwidth excites multiple longitudinal modes so we can deduce the optical cavity length (including the light's penetration in the metasurface and the reflectors) from the spectral spacing between these modes (the free spectral range λ_{FSR}). We then narrowed the incident laser bandwidth to 5 nm in order to excite only one longitudinal mode and recorded the spatial intensity distribution in the image plane and the transmitted spectrum.

Results are summarized in Figure 4. We observe transmission maxima at cavity lengths spaced by $\lambda/2$ = 316.5 nm (see Figure 4b). To judge the recreation of the designed mode, we calculated the normalized root-mean-square deviation at each resonance position, which is shown in Figure 4c. We observe the best skier image at a cavity length of 40.8 μm (compare Figure 4a,e), which is very close to the design length. In the spectral domain (see Figure 4d), the mode exhibits a bandwidth of Γ = 0.8 nm, determined by using a Lorentzian fit, which results in a quality factor of $Q \simeq 800$. The skier is also reproduced at other cavity lengths close to the design length; however, it starts deteriorating quickly and becomes indiscernible at more than ∼5 μm away from the design length (Figure 4e). Using the

https://doi.org/10.1021/acsphotonics.3c01479
ACS Photonics 2024, 11, 941–949

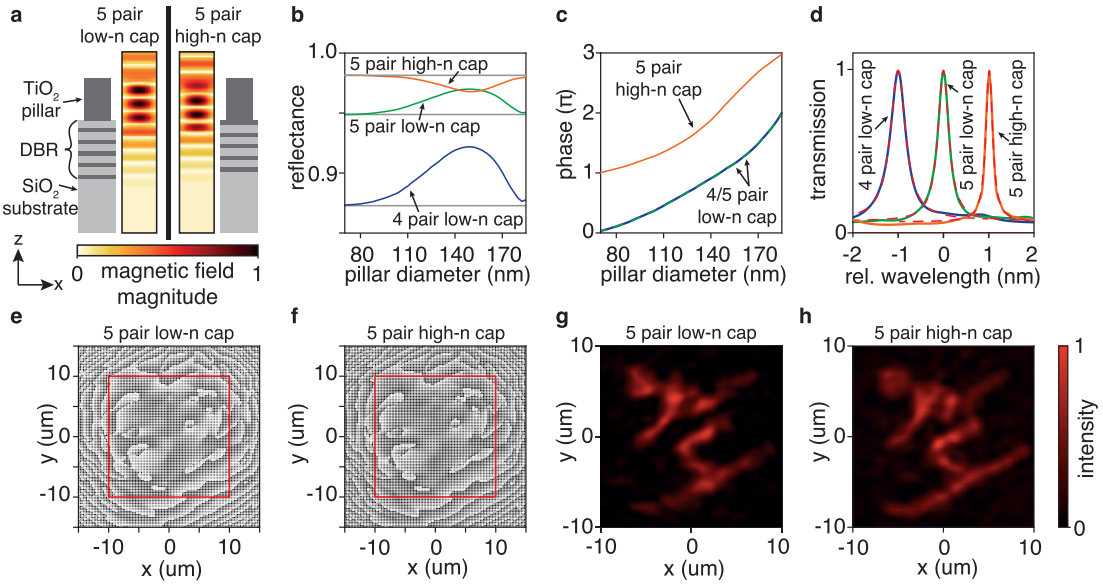

Figure 5. Employing distributed Bragg reflectors (DBRs) in complex-shaped-mode metasurface microcavities. (a) Side-view cross sections of the new metasurface unit cells comprising a circular TiO_2 nanopillar (dark gray) on a SiO_2/TiO_2 DBR on a SiO_2 substrate (light gray). The DBR can be terminated by a low-n layer (SiO_2, left panel) or a high-n layer (TiO_2, right panel). Next to the schematics, false color plots show the magnetic field of a reflected light wave that penetrates deeper into the low-n-capped DBR (633 nm wavelength, 180 nm pillar diameter, 600 nm pillar height, 250 nm × 250 nm unit cell size). (b) Diameter-dependent reflectance of nanopillars on different DBRs (colored lines). The gray lines mark the reflectance of the bare DBRs. (c) Diameter-dependent reflection phase of nanopillars on different DBRs. The reflection phases of the low-n-capped DBRs with four and five layers are indistinguishable. (d) Transmission spectra (colored lines) of skier modes modeled by full-cavity simulations implementing the metasurfaces in panels e and f (designed using the libraries in panel c). The red dashed lines are least-squares fits of a Lorentzian function to the data. (e) Metasurface design realizing a skier mode using a low-n-capped DBR. The red square marks a 20 μm × 20 μm area. (f) Metasurface design realizing a skier mode using a high-n capped DBR. (g) Spatial cavity mode profile realized using a 30 μm × 30 μm metasurface on a low-n-capped DBR (panel e). (h) Spatial cavity mode profile realized using a 30 μm × 30 μm metasurface on a high-n-capped DBR (panel f).

Table 1. Full-Cavity Simulation Results Employing Metasurfaces on Different SiO_2/TiO_2 DBRs

DBR type	R_{IP} (%)	R_{MP} (%)	L_{mirror} (%)	metasurface size (μm^2)	spectral bandwidth of the skier mode (nm)	quality factor (×1000)	$L_{round\text{-}trip}$ (%)	$L_{nonmirror}$ (%)
4-pair low-n cap	87	90	22	20 × 20	0.40	1.6	39	22
5-pair low-n cap	95	96	9	20 × 20	0.29	2.2	30	23
5-pair low-n cap	95	96	9	30 × 30	0.28	2.2	30	23
5-pair high-n cap	98	97	5	20 × 20	0.29	2.2	31	24
5-pair high-n cap	98	97	5	30 × 30	0.18	3.5	20	16

observed bandwidth and free spectral range (λ_{FSR} = 4.8 nm) at 40.8 μm cavity length, we find a round-trip loss of 64%. This corresponds well to the predicted round-trip loss of 69%, calculated from the partial reflector reflectance (46%) and the average metaatom reflectance used in the design (67%). This indicates that the intensity enhancement (2.6×) currently realized in the holographic metasurface microcavity is limited by our choice of mirror reflectance.

With mirror reflectance dominating the losses of the presented holographic cavity, smaller resonant line widths, higher quality factors, and higher field enhancement in the cavity should be achievable by switching from metallic partial reflectors to DBRs.[33] These mirrors furthermore eliminate the coupling loss due to absorption in the metallic partial reflectors.

Increasing Performance Using DBRs. To investigate the prospects of employing DBRs, we replace the gold layer in Figure 1a with DBRs composed of four and five layer-pairs, each comprising a quarter-wave layer of a high-index-material (titania, TiO_2, n_{TiO_2} = 2.35) and a quarter-wave layer of a low-index-material (fused silica, SiO_2, n_{SiO_2} = 1.46), see Figure 5a for an illustration. Results depend on the material of the DBRs' top layer (i.e., the material that touches the metasurface, see Figure 5a). We will call a DBR terminated by fused silica a low-n-capped DBR and by titania a high-n-capped DBR, where n is the refractive index.

When placing nanopillars on these DBRs, narrowband resonances appear in the pillar-dependent reflectance when using the previous unit cell size and nanopillar height (because the reflector's materials are nonabsorbing, long-lived resonances in the nanopillars are not damped, as they are by the gold mirror). To avoid these resonances, we decreased the unit cell size to 250 nm × 250 nm and increased the pillar height to 600 nm. We use a minimum pillar diameter of 70 nm and a minimum pillar spacing of 100 nm to maintain manufacturability.[36] The resulting nanopillar libraries offer complete phase coverage and a smooth phase and reflectance profile (Figure 5b,c). The number of layer pairs in the DBR controls the average reflectance. Still, it leaves the nanopillar-dependent reflection phase unchanged (Figure 5c). Changing the capping layer material introduces an expected π-phase shift.[37]

Picking from the three displayed libraries, we design metasurfaces to realize skier cavity modes (shown in Figure 5e,f), implement them in complete cavities, and model their

https://doi.org/10.1021/acsphotonics.3c01479
ACS Photonics 2024, 11, 941−949

performance under plane-wave illumination using finite-difference time-domain simulations. We observe Lorentzian spectral mode profiles for all mirror configurations (Figure 5d). Using a 30 μm × 30 μm size metasurface placed on a high-n-capped DBR, we achieve a designer-cavity-mode with a spectral line width of 0.18 nm, a quality factor larger than 3500, and a close reproduction of the target spatial profile (compare Figure 5h with Figure 4a).

Table 1 summarizes the bandwidths, quality factors, and round-trip losses[38] for cavities using different sizes and mirror configurations. The data reveal that the high-n-capped DBRs perform better than their low-n-capped counterparts. This observation is corroborated by the image quality (compare Figure 5g,h): although all cavities create a skier mode, the high-n-capped DBR cavity's rendition of the skier shows less speckle and its outline is truer to the design image.

DBR Subtleties in Metasurface Microcavities. To understand this difference, we explore the different loss mechanisms in a metasurface microcavity: Light is lost when it transmits through the cavity end mirrors. Our cavities comprise a metasurface-covered DBR (reflectance: R_{MP}) and an opposing DBR (reflectance: R_{IP}), yielding a total mirror loss per round-trip $L_{mirror} = 1 - R_{IP}R_{MP}$. Light is also lost when it diffracts outside the cavity (diffraction loss L_{diffr}) due to insufficient mirror size. Employing a larger metasurface mitigates this loss mechanism. Furthermore, light can be scattered outside the cavity, e.g., by phase errors introduced by the metasurface (scattering loss L_{scat}). Combined, the round-trip loss is

$$\begin{aligned} L_{\text{round-trip}} &= 1 - (1 - L_{\text{mirror}})(1 - L_{\text{diffr}})(1 - L_{\text{scat}}) \\ &= 1 - (1 - L_{\text{mirror}})(1 - L_{\text{nonmirror}}) \end{aligned} \quad (8)$$

where, on the second line, the nonmirror loss $L_{nonmirror}$ comprises the diffraction and scattering losses.

The results in Table 1 reveal that for all 20 μm × 20 μm large metasurfaces, the nonmirror losses are approximately 23%. Increasing the metasurface size to 30 μm × 30 μm should decrease the diffraction loss from 13% to 2% (and thus the nonmirror loss to approximately 14%) and improve performance. Interestingly, the performance only increases for the high-n-capped cavity and remains unchanged for the low-n-capped cavity. Because the metasurface designs are alike (compare Figure 5e,f), the root cause must be the DBRs: light penetrates deeper into a low-n-capped DBR than into a high-n-capped DBR.[37,39] This fact holds when a metasurface is on the DBR, as visible in the field distributions plotted in Figure 5a.

When increasing the metasurface size, we add regions (see the areas outside of the red squares in Figure 5e,f) that require steep phase profiles (much like the outside parts of a lens with a high numerical aperture). In these regions, neighboring nanopillars must introduce phase differences larger than those in the center of the metasurface and are less similar. When the light penetrates the DBR, it is unconfined (unlike in the metasurface's titania nanopillars) and is more prone to mix with light from the neighboring unit cells. Consequently, due to their lower light penetration, high-n-capped DBRs allow less mixing between the light fields of adjacent metasurface unit cells and can implement higher phase slopes, explaining their better performance and image quality. This finding extends beyond implementing microcavities and should also be taken into consideration when designing other metasurface−DBR hybrid reflectors.

For small spectral bandwidths, which are common in cavity applications, and simple mode profiles, scattering losses at the percent level have been realized.[24] The rapid progress in novel design techniques and optical metasurfaces[40] promises similar efficiencies for complex-shaped mode profiles and broader bandwidths in the near future.

CONCLUSION

Previous microcavities have focused on simple mode shapes due to fabrication limitations. Free-form mode profiles have so far relied on injecting an image and macroscopic setups to achieve imaging functionality.[11−13] As shown, the holographic metasurface microcavity uses the design flexibility and miniature scale of optical metasurfaces to fulfill the round-trip condition for a complex-shaped mode profile.

The presented design mechanism can realize arbitrary and asymmetric mode profiles within physical limits: First, the minimal achievable feature size in the image plane is given by the size of the metasurface and is limited by the Abbe diffraction limit. This can effectively be overcome as metasurfaces today can be manufactured with centimeter scale and larger transverse dimensions[41,42] and at ultraviolet frequencies.[43−46] If a use case requires changing conserved quantities of the incoming light, e.g., its orbital angular momentum (OAM),[47] two different metasurface partial reflectors are required to maintain an intact round-trip phase condition.

We foresee that holographic metasurface microcavities could be useful for various applications.

Semiconductor lasers, including quantum dot lasers,[48] quantum-cascade lasers,[49] and vertical-cavity surface-emitting lasers, have nonspherical intracavity modes and output modes due to their geometry. Holographic microcavities can optimally illuminate the nonspherical gain materials in such lasers by shaping their intracavity spatial mode profile. They can also efficiently couple such lasers to external microcavities or provide spatially tailored feedback, e.g., to balance the thermal load in such lasers.

Optical lattices are established by standing wave patterns formed by counterpropagating light beams. Cavities enhance such standing waves.[50] Currently, modes with large diameters are employed to increase the intensity uniformity at their center. When two metasurface reflectors are used, our approach can create an image plane in the free space between them. A cavity hologram can then increase the mode uniformity to miniaturize the optical lattice assembly or to shape the optical lattice.

Microscale intracavity image enhancement could also potentiate optical signal processing, as has been previously suggested.[13] By adding a thin or two-dimensional nonlinear material in the image plane of the metacavity and tailoring the holographic mode to couple spatially separate spots of the nonlinear material, optical thresholding depending on multiple input parameters[51] could be realized. This capability would be helpful, e.g., for optical artificial neural networks.

Furthermore, cavity-enhanced microscopy promises to enhance detection sensitivity via multiple light−matter interactions[6] or the Purcell effect.[52] Holographic microcavities could combine sensitivity enhancement with structured illumination by light sheets or Bessel beams.

Our solution uses widespread and industrially scalable fabrication protocols and thus can directly be adopted at an industry scale.

https://doi.org/10.1021/acsphotonics.3c01479
ACS Photonics 2024, 11, 941−949

AUTHOR INFORMATION

Corresponding Author

Marcus Ossiander − *John A. Paulson School of Engineering and Applied Sciences, Harvard University, Cambridge, Massachusetts 02138, United States; Institute of Experimental Physics, Graz University of Technology, 8010 Graz, Austria;* orcid.org/0000-0001-5925-8768; Email: mossiander@g.harvard.edu

Authors

Sydney Mason − *John A. Paulson School of Engineering and Applied Sciences, Harvard University, Cambridge, Massachusetts 02138, United States;* Present Address: E.L. Ginzton Laboratory, Stanford University, Stanford, California 94305, United States

Maryna Leonidivna Meretska − *John A. Paulson School of Engineering and Applied Sciences, Harvard University, Cambridge, Massachusetts 02138, United States;* Present Address: Institute of Nanotechnology, Karlsruhe Institute of Technology (KIT), 76344 Eggenstein-Leopoldshafen, Germany

Christina Spägele − *John A. Paulson School of Engineering and Applied Sciences, Harvard University, Cambridge, Massachusetts 02138, United States*

Federico Capasso − *John A. Paulson School of Engineering and Applied Sciences, Harvard University, Cambridge, Massachusetts 02138, United States*

Complete contact information is available at: https://pubs.acs.org/10.1021/acsphotonics.3c01479

Author Contributions

S.M. and M.O. developed the project. S.M. designed the metasurface. M.L.M. fabricated the samples. S.M. imaged the samples. S.M., C.S., and M.O. built the experimental setup and experimented. S.M. and M.O. performed numerical modeling. S.M., M.O., and F.C. wrote the manuscript.

Funding

This work was performed, in part, at the Center for Nanoscale Systems (CNS), a member of the National Nanotechnology Coordinated Infrastructure (NNCI), which is supported by the NSF under award no. ECCS-2025158. CNS is a part of Harvard University. The authors acknowledge partial financial support from the Air Force Office of Scientific Research (AFOSR), under award number FA9550-21-1-0312. M.O. acknowledges funding by the Alexander von Humboldt Foundation (Feodor-Lynen Fellowship), by the Austrian Science Fund (FWF) Start Grant Y1525, and by the European Union (grant agreement 101076933 EUVORAM). For the purpose of open access, the authors have applied a CC BY public copyright license to any Author Accepted Manuscript version arising from this submission. Views and opinions expressed are however those of the author(s) only and do not necessarily reflect those of the European Union or the European Research Council Executive Agency. Neither the European Union nor the granting authority can be held responsible for them.

Notes

The authors declare no competing financial interest.

ACKNOWLEDGMENTS

The authors acknowledge a Tidy3d computation power gift from Zongfu Yu at Flexcompute Inc.

REFERENCES

(1) Vahala, K. J. Optical microcavities. *Nature* **2003**, *424* (6950), 839−846.

(2) Gu, Q.; Fainman, Y. Purcell Effect and the Evaluation of Purcell and Spontaneous Emission Factors. In *Semiconductor Nanolasers*; Cambridge University Press, 2017; pp 65−90.

(3) Garcia-Vidal, F. J.; Ciuti, C.; Ebbesen, T. W. Manipulating matter by strong coupling to vacuum fields. *Science* **2021**, *373* (6551), eabd0336.

(4) Bergstein, D. A.; Özkumur, E.; Wu, A. C.; Yalçin, A.; Colson, J. R.; Needham, J. W.; Irani, R. J.; Gershoni, J. M.; Goldberg, B. B.; DeLisi, C.; Ruane, M. F.; Ünlü, M. S. Resonant Cavity Imaging: A Means Toward High Throughput Label-Free Protein Detection. *IEEE J. Sel. Top. Quantum Electron.* **2008**, *14* (1), 131−139.

(5) Armani, A. M.; Kulkarni, R. P.; Fraser, S. E.; Flagan, R. C.; Vahala, K. J. Label-Free, Single-Molecule Detection with Optical Microcavities. *Science.* **2007**, *317* (5839), 783−787.

(6) Mader, M.; Reichel, J.; Hänsch, T. W.; Hunger, D. A scanning cavity microscope. *Nat. Commun.* **2015**, *6*, 7249.

(7) Ye, J.; Vernooy, D.; Kimble, H. Trapping of Single Atoms in Cavity QED. *Phys. Rev. Lett.* **1999**, *83* (24), 4987−4990.

(8) Thompson, J. D.; Tiecke, T. G.; de Leon, N. P.; Feist, J.; Akimov, A. V.; Gullans, M.; Zibrov, A. S.; Vuletić, V.; Lukin, M. D. Coupling a Single Trapped Atom to a Nanoscale Optical Cavity. *Science* **2013**, *340* (6137), 1202−1205.

(9) Trichet, A. A. P.; Dolan, P. R.; Coles, D. M.; Hughes, G. M.; Smith, J. M. Topographic control of open access microcavities at the nanometer scale. *Opt. Express* **2015**, *23* (13), 17205−17216.

(10) Chen, Y.-J.; Zigo, S.; Raithel, G. Atom trapping and spectroscopy in cavity-generated optical potentials. *Phys. Rev. A* **2014**, *89* (6), No. 063409.

(11) Pole, R. V.; Wieder, H.; Barrekette, E. S. Reactive Optical Information Processing. I: Theory of Information Recovery and Resonator Mode Structure. *Appl. Opt.* **1967**, *6* (9), 1571−1575.

(12) Riazi, A.; Gandhi, O. P.; Christensen, D. A. Imaging characteristics of a confocal cavity. *Opt. Commun.* **1979**, *28* (2), 163−165.

(13) Ryou, A.; Colburn, S.; Majumdar, A. Image amplification in a self-imaging degenerate optical cavity. *Phys. Rev. A* **2020**, *101* (1), No. 013824.

(14) Sihvola, A. Metamaterials in electromagnetics. *Metamaterials* **2007**, *1* (1), 2−11.

(15) Li, A.; Singh, S.; Sievenpiper, D. Metasurfaces and their applications. *Nanophotonics* **2018**, *7* (6), 989−1011.

(16) Lim, S. W. D.; Park, J. S.; Meretska, M. L.; Dorrah, A. H.; Capasso, F. Engineering phase and polarization singularity sheets. *Nat. Commun.* **2021**, *12*, 4190.

(17) Khorasaninejad, M.; Chen, W. T.; Devlin, R. C.; Oh, J.; Zhu, A. Y.; Capasso, F. Metalenses at visible wavelengths: Diffraction-limited focusing and subwavelength resolution imaging. *Science* **2016**, *352* (6290), 1190−1194.

(18) Ni, X.; Kildishev, A. V.; Shalaev, V. M. Metasurface holograms for visible light. *Nat. Commun.* **2013**, *4*, 2807.

(19) Spägele, C.; Tamagnone, M.; Kazakov, D.; Ossiander, M.; Piccardo, M.; Capasso, F. Multifunctional wide-angle optics and lasing based on supercell metasurfaces. *Nat. Commun.* **2021**, *12*, 3787.

(20) Fong, B. H.; Colburn, J. S.; Ottusch, J. J.; Visher, J. L.; Sievenpiper, D. F. Scalar and Tensor Holographic Artificial Impedance Surfaces. *IEEE Trans. Antennas Propag.* **2010**, *58* (10), 3212−3221.

(21) Kim, K.-J.; Park, B.-S.; Kim, J.-K.; Kim, D.-W.; Seo, Y.-H. Holographic augmented reality based on three-dimensional volumetric imaging for a photorealistic scene. *Opt. Express* **2020**, *28* (24), 35972−35985.

(22) Qu, G.; Yang, W.; Song, Q.; Liu, Y.; Qiu, C.-W.; Han, J.; Tsai, D.-P.; Xiao, S. Reprogrammable meta-hologram for optical encryption. *Nat. Commun.* **2020**, *11*, 5484.

(23) Fu, J.; Jin, Y.; He, S. Metasurface for Constructing a Stable High-Q Plano-Planar Open Cavity. *Adv. Opt. Mater.* **2019**, *7* (5), No. 1801339.

(24) Ossiander, M.; Meretska, M. L.; Rourke, S.; Spägele, C.; Yin, X.; Benea-Chelmus, I.-C.; Capasso, F. Metasurface-stabilized optical microcavities. *Nat. Commun.* **2023**, *14*, 1114.
(25) Flannery, J.; Al Maruf, R.; Yoon, T.; Bajcsy, M. Fabry-Pérot Cavity Formed with Dielectric Metasurfaces in a Hollow-Core Fiber. *ACS Photonics* **2018**, *5* (2), 337−341.
(26) Li, Y.; Kita, S.; Muñoz, P.; Reshef, O.; Vulis, D. I.; Yin, M.; Lončar, M.; Mazur, E. On-chip zero-index metamaterials. *Nat. Photonics* **2015**, *9*, 738−742.
(27) Shaltout, A. M.; Kim, J.; Boltasseva, A.; Shalaev, V. M.; Kildishev, A. V. Ultrathin and multicolour optical cavities with embedded metasurfaces. *Nat. Commun.* **2018**, *9*, 2673.
(28) Xie, Y. Y.; Ni, P. N.; Wang, Q. H.; Kan, Q.; Briere, G.; Chen, P. P.; Zhao, Z. Z.; Delga, A.; Ren, H. R.; Chen, H. D.; Xu, C.; Genevet, P. Metasurface-integrated vertical cavity surface-emitting lasers for programmable directional lasing emissions. *Nat. Nanotechnol.* **2020**, *15*, 125−130.
(29) Ratni, B.; Merzouk, W. A.; de Lustrac, A.; Villers, S.; Piau, G. P.; Burokur, S. N. Design of Phase-Modulated Metasurfaces for Beam Steering in Fabry-Perot Cavity Antennas. *IEEE Antennas and Wireless Propagation Letters* **2017**, *16*, 1401−1404.
(30) Wei, Y.; Zhao, M.; Yang, Z. Silicon metasurface embedded Fabry-Perot cavity enables the high-quality transmission structural color. *Opt. Lett.* **2022**, *47* (20), 5344−5347.
(31) Chen, Q. Y.; Liu, F. R.; Zhang, Y. Z.; Zhang, L. L.; Lian, B. Y.; Yin, B. S. Simulations of a Wide-Gamut and Angle-Dependent Color Reflector by Addition of a Nanometer-Thick Interference Medium in a Fabry-Perot Structure. *ACS Appl. Nano Mater.* **2023**, *6* (15), 14583−14593.
(32) Spaegele, C.; Capasso, F.; Tamagnone, M. Open Optical Cavities based on Metasurfaces. *Reviews of Electromagnetics* **2022**, *1*, 1−3.
(33) Jin, N.; McLemore, C. A.; Mason, D.; Hendrie, J. P.; Luo, Y.; Kelleher, M. L.; Kharel, P.; Quinlan, F.; Diddams, S. A.; Rakich, P. T. Micro-fabricated mirrors with finesse exceeding one million. *Optica* **2022**, *9* (9), 965−970.
(34) Devlin, R. C.; Khorasaninejad, M.; Chen, W. T.; Oh, J.; Capasso, F. Broadband high-efficiency dielectric metasurfaces for the visible spectrum. *Proc. Natl. Acad. Sci. U. S. A.* **2016**, *113* (38), 10473−10478.
(35) Gerchberg, R. W. A Practical Algorithm for the Determination of Phase from Image and Diffraction Plane Pictures. *Optik* **1972**, *35*, 237−246.
(36) Chen, W. T.; Zhu, A. Y.; Sisler, J.; Bharwani, Z.; Capasso, F. A broadband achromatic polarization-insensitive metalens consisting of anisotropic nanostructures. *Nat. Commun.* **2019**, *10*, 355.
(37) Brovelli, L. R.; Keller, U. Simple analytical expressions for the reflectivity and the penetration depth of a Bragg mirror between arbitrary media. *Optical Communications* **1995**, *116* (4−6), 343−350.
(38) Suter, M.; Dietiker, P. Calculation of the finesse of an ideal Fabry-Perot resonator. *Appl. Opt.* **2014**, *53* (30), 7004−7010.
(39) Koks, C.; van Exter, M. P. Microcavity resonance condition, quality factor, and mode volume are determined by different penetration depths. *Opt. Express* **2021**, *29* (5), 6879−6889.
(40) He, Q.; Sun, S.; Xiao, S.; Zhou, L. High-Efficiency Metasurfaces: Principles, Realizations, and Applications. *Adv. Opt. Mater.* **2018**, *6* (19), No. 1800415.
(41) Park, J.-S.; Lim, S. W. D.; Amirzhan, A.; Kang, H.; Karrfalt, K.; Kim, D.; Leger, J.; Urbas, A. M.; Ossiander, M.; Li, Z.; Capasso, F. All-glass 100 mm Diameter Visible Metalens for Imaging the Cosmos. *ACS Nano* **2024**, *18*, 3187.
(42) Li, Z.; Pestourie, R.; Park, J. S.; Huang, Y. W.; Johnson, S. G.; Capasso, F. Inverse design enables large-scale high-performance meta-optics reshaping virtual reality. *Nat. Commun.* **2022**, *13*, 2409.
(43) Tseng, M. L.; Semmlinger, M.; Zhang, M.; Arndt, C.; Huang, T.-T.; Yang, J.; Kuo, H. Y.; Su, V.-C.; Chen, M. K.; Chu, C. H.; Cerjan, B.; Tsai, D. P.; Nordlander, P.; Halas, N. J. Vacuum ultraviolet nonlinear metalens. *Sci. Adv.* **2022**, *8*, 16.
(44) Zhang, C.; Divitt, S.; Fan, Q.; Zhu, W.; Agrawal, A.; Lu, Y.; Xu, T.; Lezec, H. J. Low-loss metasurface optics down to the deep ultraviolet region. *Light Sci. Appl.* **2020**, *9*, 55.
(45) Ossiander, M.; Meretska, M. L.; Hampel, H. K.; Lim, S. W. D.; Knefz, N.; Jauk, T.; Capasso, F.; Schultze, M. Extreme ultraviolet metalens by vacuum guiding. *Science* **2023**, *380* (6640), 59−63.
(46) Huang, K.; Deng, J.; Leong, H. S.; Yap, S. L. K.; Yang, R. B.; Teng, J.; Liu, H. Ultraviolet Metasurfaces of ≈80% Efficiency with Antiferromagnetic Resonances for Optical Vectorial Anti-Counterfeiting. *Laser Photonics Rev.* **2019**, *13* (5), No. 1800289.
(47) Shen, Y.; Wang, X.; Xie, Z.; Min, C.; Fu, X.; Liu, Q.; Gong, M.; Yuan, X. Optical vortices 30 years on: OAM manipulation from topological charge to multiple singularities. *Light Sci. Appl.* **2019**, *8*, 90.
(48) Liu, A. Y.; Srinivasan, S.; Norman, J.; Gossard, A. C.; Bowers, J. E. Quantum dot lasers for silicon photonics [Invited]. *Photon. Res.* **2015**, *3*, B1−B9.
(49) Vitiello, M. S.; Tredicucci, A. Physics and technology of Terahertz quantum cascade lasers. *Advances in Physics: X* **2021**, *6* (1), 1893809.
(50) Heinz, A.; Trautmann, J.; Šantić, N.; Park, A. J.; Bloch, I.; Blatt, S. Crossed optical cavities with large mode diameters. *Opt. Lett.* **2021**, *46* (2), 250−253.
(51) Williamson, I. A. D.; Hughes, T. W.; Minkov, M.; Bartlett, B.; Pai, S.; Fan, S. Reprogrammable Electro-Optic Nonlinear Activation Functions for Optical Neural Networks. *IEEE J. Sel. Top. Quantum Electron.* **2020**, *26* (1), 7700412.
(52) Hümmer, T.; Noe, J.; Hofmann, M. S.; Hänsch, T. W.; Högele, A.; Hunger, D. Cavity-enhanced Raman microscopy of individual carbon nanotubes. *Nat. Commun.* **2016**, *7*, 12155.

https://doi.org/10.1021/acsphotonics.3c01479
ACS Photonics 2024, 11, 941−949